

Effects of resistance on spatiotemporal variables and electromyographic activity of the hamstrings during maximal sprint acceleration

Original

Effects of resistance on spatiotemporal variables and electromyographic activity of the hamstrings during maximal sprint acceleration / Dániel, Csala; Martins, Taian; János, Tóth; Örs, Sebestyén; József, Tihanyi; András, Hegyi. - In: PHYSIOLOGY INTERNATIONAL. - ISSN 2498-602X. - (2026). [10.1556/2060.2026.00745]

Availability:

This version is available at: 11583/3010595 since: 2026-05-06T10:46:32Z

Publisher:

Akademiai Kiado

Published

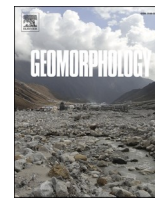
DOI:10.1556/2060.2026.00745

Terms of use:

This article is made available under terms and conditions as specified in the corresponding bibliographic description in the repository

Publisher copyright

(Article begins on next page)



Does bed relief index inform about sediment supply in proglacial multi-channel systems? The Rutor case study (Italian Alps)

E. Corte^{a,*}, M.M. Macelloni^a, S. Tamea^a, C. Camporeale^a, H. Piégay^b

^a Department of Environment, Land and Infrastructure Engineering (DIATI), Politecnico di Torino, Corso Duca degli Abruzzi 24, 10129, Torino, Italy

^b CNRS, UMR 5600 Environnement Ville Société (EVS), École Normale Supérieure de Lyon, Université de Lyon, 15 Parvis René Descartes, 69342, Lyon Cedex 07, France

ARTICLE INFO

Keywords:
Proglacial area
Delta
Braided river
European Alps

ABSTRACT

This study examines links between proglacial river-reach morphology and glacier dynamics at Rutor Glacier (Italian Alps). High-resolution photogrammetric DSMs (2021–2023) were used to compute the Bed Relief Index (BRI^*) across six proglacial multi-channel systems. BRI^* distinguishes sediment-starved from transport-limited morphologies; here we test its value for diagnosing spatial and temporal contrasts in sediment availability and transport regime across proglacial reaches. BRI^* shows strong relationships with reach slope and active channel width, emphasizing their role in shaping proglacial morphodynamics. To improve cross-reach comparability, we develop a normalization approach that removes slope and width effects, producing a normalized BRI^* suited to contrasting systems with different gradients and channel dimensions. Results reveal a spatial mosaic of transport-limited and sediment-supply-limited conditions, indicating strong variability in sediment availability. Planform type (fan-shaped versus linear) does not systematically control reach response, whereas delta reaches differ because their dynamics are primarily constrained by downstream base level. Several reaches exhibit elevated BRI^* values consistent with modest sediment starvation linked to reduced glacial input and disconnection from upstream lakes. Normalized BRI^* enables direct comparison with two braided reaches in France and yields consistent discrimination of transport regimes. Overall, BRI^* —especially when normalized—provides a practical diagnostic of sediment-transport conditions in proglacial multi-channel systems, supporting continued monitoring to capture longer-term adjustments under changing boundary conditions.

1. Introduction

In proglacial environments, gravel-bed multi-channel systems such as braided sections, outwash plains, fans and deltas are crucial for sediment redistribution and landscape evolution (Carrivick and Tweed, 2013; Matthews, 2019). Braided proglacial rivers receive high sediment loads from glacial meltwater, forming unstable channels that frequently adjust due to seasonal and climatic variations (Matthews, 2019). Where proglacial outwash is laterally unconfined, meltwater deposition forms broad outwash plains that typically host sediment-rich braided networks under highly variable discharge regimes (Maizels, 2002; Carrivick and Rushmer, 2009; Carrivick and Russell, 2013). Proglacial alluvial/outwash fans form where meltwater channels emerge from confined reaches onto the forefield, and their geometry reflects the balance between discharge and sediment calibre (Le Hooke and Rohrer, 1979). On these fans, channel patterns can shift rapidly in response to changes in discharge, grain size, and base-level conditions, leading to pronounced

planform reorganization over short timescales (De Jong, 1992). Proglacial deltas, accumulating sediments from glacial outflows, serve as natural archives of environmental change, recording fluctuations in sediment supply, glacial retreat, and lake infill dynamics (Dirszowsky and Desloges, 2004; Winsemann et al., 2018; Normandeau et al., 2019). These deltas act as efficient sediment traps, influencing lake evolution and long-term basin infill rates (Carrivick and Tweed, 2013). However, despite their significance, the morphodynamics of proglacial deltas remain understudied, with most research focusing on large fjord or proglacial lake settings to reconstruct paleoenvironments or predict future change (Winsemann et al., 2018; Normandeau et al., 2019).

Alpine proglacial environments are often remote, characterized by steep slopes, unstable terrain, and high-energy flows. These aspects make direct field measurements hazardous and logistically difficult (Sanders et al., 2013; Matthews, 2019). Traditional methods for assessing sediment transport and river morphology often rely on in-situ surveys, which may be impractical in such settings (Morche et al., 2015;

* Corresponding author.

E-mail address: elisabetta.corte@polito.it (E. Corte).

Carrivick and Heckmann, 2017; Delaney et al., 2024; Mancini et al., 2024). In recent decades, the application of remote sensing techniques has significantly advanced the monitoring of proglacial areas, enabling the multi-temporal mapping of landform evolution and the quantification of sediment budgets over large or inaccessible regions (Carrivick et al., 2018; Piermattei et al., 2023; Savi et al., 2024). These studies typically employ high-resolution data to perform geomorphic change detection through the comparison of surface models, allowing for a detailed understanding of erosion and deposition patterns without the risks associated with ground-based surveys (Morche et al., 2015; Mancini et al., 2023). Topographic indices derived from high-resolution remote sensing data, such as digital elevation models (DSMs), allow for the quantification of geomorphic change in these contexts while avoiding crossing channels of interest.

Braided river behaviors are analyzed using a variety of indices and indicators that focus on different aspects of their structure and function (Bridge, 1993; Friend and Sinha, 1993; Egozi and Ashmore, 2008; Belletti et al., 2013). Indicators for assessing braided river physical functioning are essential for understanding their dynamics and ecological patterns (Ferguson, 1993; Ashmore, 2013; Belletti et al., 2013). These indicators can be related to hydraulic geometry (Ashmore and Sauks, 2006; Morel et al., 2019), channel planform characters (Bridge, 1993; Belletti et al., 2013), surface vs subsurface water interactions (Belletti et al., 2013), and vegetation dynamics (Lallias-Tacon et al., 2017).

Among the many available indices, the Normalized Bed Relief Index (BRI^*) has been applied in river restoration and morphodynamic studies as a tool to assess the macro-roughness and sediment transport dynamics of braided rivers, providing a dimensionless indicator of sediment regime. BRI^* is conceptually rooted in the Bed Relief Index (BRI) introduced in laboratory experiments on braided-channel morphology and bedload pulses, where BRI is defined as the standard deviation of bed elevations around the mean bed elevation within the active channel portion of a cross-section (Hoey and Sutherland, 1991). Building on this concept, Liébault et al. (2013) introduced the normalized formulation (BRI^*), where BRI is normalized by the active channel width (ACW). BRI^* has since been used to diagnose reach-scale sediment regime and morphodynamic state in braided rivers, and to document responses to sediment-supply alteration and restoration, often in combination with width-based metrics (Liébault et al., 2013; Chapuis et al., 2018; Brousse et al., 2021; Devreux et al., 2022). In these applications, higher BRI^* generally reflects a rougher, more incised morphology trending toward a single-thread configuration, whereas lower values are associated with aggradation and a more laterally distributed multi-channel pattern (Liébault et al., 2013; Devreux et al., 2022).

Despite these advances, the applicability of BRI^* to proglacial multi-channel systems (outwash plains, fans, and deltas) remains largely untested, and it is unclear whether BRI^* retains a consistent sensitivity to sediment supply versus transport capacity in such rapidly evolving settings. Here we evaluate BRI^* in a set of proglacial multi-channel reaches of the Rutor forefield (Italian Alps) using multi-temporal high-resolution DSMs. Specifically, this study aims to (i) quantify BRI^* from multi-temporal high-resolution DSMs across proglacial multi-channel systems and survey years, and (ii) test whether BRI^* can discriminate contrasting sediment-regime conditions (transport-limited vs supply-limited) within and among these systems. We further aim to evaluate how strongly BRI^* is controlled by key covarying geomorphic factors (active-channel width and slope) and assess whether a combined normalization accounting for these factors provides a repeatable remote-sensing indicator for proglacial settings where field measurements are difficult or unsafe.

2. Case study

The Rutor Glacier, situated at the head of the Dora Baltea Valley, near the French-Italian border in northwestern Italy, is one of the largest glaciers in the Italian Alps and the third largest in the Aosta Valley.

Located at altitudes between 2540 m and 3481 m above sea level, the glacier spans an area of approximately 7.5 km². Historically a single continuous ice body, its terminus now forms three distinct tongues, showing significant retreat since the mid-19th century (Villa et al., 2007). Since the Little Ice Age maximum, the glacier has lost about 34% of its surface area, with retreat and surface lowering most pronounced in its eastern tongue (Macelloni et al., 2022; Corte et al., 2024).

The glacier's mass balance, monitored by the Valle d'Aosta Regional Environmental Protection Agency (ARPA) since 2005, has been predominantly negative, resulting in a net loss of −12,252 mm water equivalent by 2017. The proglacial area of the Rutor Glacier now covers approximately 4 km², featuring diverse geomorphological formations such as steep slopes, outwash plains, deltas, and braided to single-channel systems. This landscape, composed of sediments ranging from fine clays to large boulders, provides an exceptional natural laboratory for investigating sediment dynamics and proglacial fluvial processes. Its minimal human disturbance further enhances its value as a study site for understanding glacier-driven geomorphological changes.

The Rutor proglacial area, located within a dynamic glacial environment, encompasses six distinct fluvial systems: four deltas/fans, one outwash plain, and one braided river, identified sequentially from downstream to upstream as S1 through S6 (Fig. 1). The designations “S” stand for “system”, followed by a numerical identifier that reflects the system's position within the broader proglacial area.

Each system within this proglacial landscape exhibits unique geomorphological characteristics, influenced by its position relative to the glacier, the nature of sediment supply, and the dynamics of meltwater flow.

S6 is a delta covering an area of approximately 9000 m² and is fed by meltwater from the left tongue of the glacier. S6 is particularly notable for the presence of several subsurface flows, where channels appear to originate directly from sediment bars due to upwelling, as observed in orthophotographic imagery, demonstrating the low section functions as a delta. These subsurface flow paths add complexity to sediment transport and deposition processes within the reach.

S5 flows into a lake and is therefore classified as a delta but its slope is very high, indicating that it is more a fan than a delta. This system is fed by meltwater from the central tongue of the glacier and has undergone significant morphological changes in recent years. In 2021 and 2022, S5 covered an area of approximately 1000 m². However, in 2023, the upstream portion of the system expanded dramatically—by roughly 400%—reaching a total area of about 5400 m². The system is entirely unvegetated, which is consistent with its recent exposure; S5 is the third most recent system to emerge due to glacier retreat.

S4 is a braided reach, located directly in front of the right tongue of the glacier; between 2021 and 2023, its area increased from approximately 2600 m² to about 5200 m². Unlike the other reaches, S4 is directly fed by meltwater distributed along its entire upstream side and has a cross-slope of approximately 1.4%.

Delta S3 covers an area of approximately 15,000 m² and is fed by a single stream that conveys meltwater from the right tongue of the glacier. S3 has a deltaic geometry and flows into a lake. S3 is the closest delta to the glacier front and the second-closest system overall. The area is entirely unvegetated, likely due to its recent formation.

S2 is a proglacial outwash plain covering approximately 44,000 m² upstream of S1. This system receives meltwater from all glacier tongues via four distinct inflow channels. The northeastern portion of S2, referred to as S2veg, is primarily fed by the right glacier tongue and is characterized by significant vegetation cover. In contrast, the southwestern portion, termed S2noveg, is nourished by meltwater from the middle and left glacier tongues and exhibits minimal vegetation.

Beyond vegetation differences, the two sectors also diverge in the spatial arrangement of their channel networks. In the S2veg area, the distributary channels radiate outward from a single channel, creating a broadly divergent pattern. In contrast, S2noveg exhibits a more longitudinal organization, with channels aligned predominantly along the

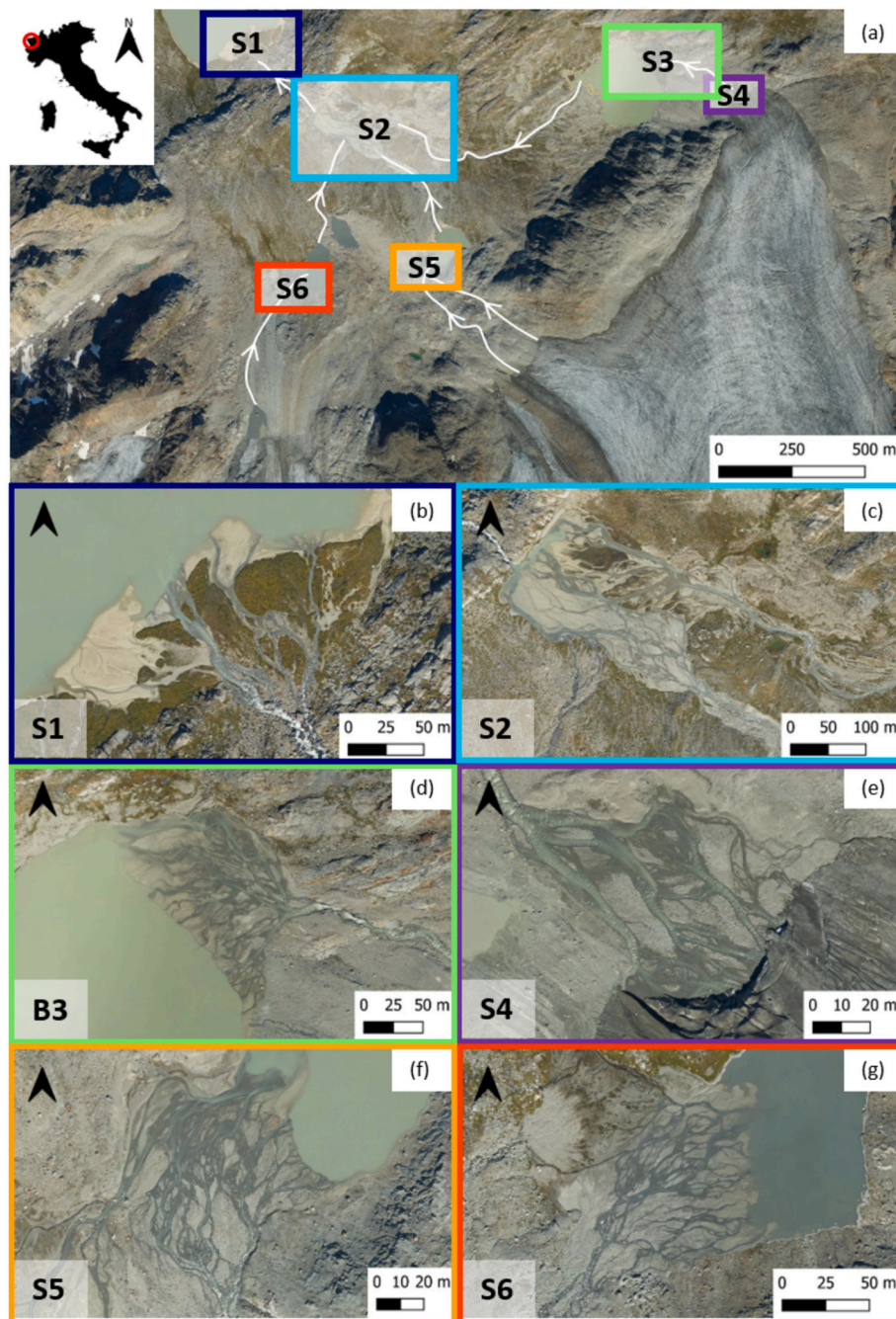


Fig. 1. Overview of the study area: (a) Orthophotos of a portion of the Rutor proglacial area showing the location of the six investigated systems (colored rectangles). The white lines and arrowheads indicate the main meltwater channels and their respective flow directions. (b–g) Detailed views of the six systems corresponding to the enlarged rectangles in panel (a).

main flow direction. Given these morphological and hydrological contrasts, S2veg and S2noveg are treated as distinct analytical units in subsequent analyses.

System S1 is the most downstream delta/fan in the proglacial sequence and spans an area of approximately 17,000 m². This reach is primarily fed by a single, steeply sloping stream with a gradient of 46.6%. The contributing stream conveys meltwater from the entire Rutor glacier, providing a substantial hydrological input. The active area of S1 is the most densely vegetated among the studied systems. Upstream, S1 shows a relatively steep gradient and a fan-like planform, with distributary channels that diverge downstream and show limited rejoining even near the lake margin, consistent with fan-delta settings where distributary networks are poorly developed; this contrasts with

lacustrine deltas, where deposition and planform are strongly structured by downstream base-level control and stream deceleration at the lake interface (Galloway, 1991; Patranabis-Deb and Chaudhuri, 2007; Carivick and Tweed, 2013).

Table 1 summarizes the key characteristics of the systems over the three years studied acquisitions, including elongation (length/width of the active channel corridor, *E*), water width (*WW*), *ACW*, slope (*S*), and vegetation coverage (*Veg*).

3. Methodology

The methodology focuses on calculating the *BRI** to assess morphological conditions in six different proglacial systems using high-

Table 1

Summary of characteristics of the fluvial systems (Sys) over time. *E* = elongation; *WW* = mean water width (m); *ACW* = mean active-channel width (m); *S* = reach-averaged slope (%); *Veg* = vegetation cover (%). The last column provides a concise, qualitative sediment characterization for each system based on field observations and interpretation of orthophotographic imagery.

Sys	Year	<i>E</i>	<i>WW</i> (m)	<i>ACW</i> (m)	<i>S</i> (%)	<i>Veg</i> (%)	Sediment characteristic
S6	2021	1.88	17.15	67.20	6.12	0.03	Heterogeneous: coarser material mainly upstream, with progressive downstream fining.
	2022	1.82	6.960	70.84	6.06	0.03	
	2023	1.75	16.25	69.66	6.09	0.11	
S5	2021	1.58	5.34	24.81	6.17	0.00	Heterogeneous: coarser material mainly upstream, with progressive downstream fining.
	2022	1.59	1.96	24.82	6.19	0.00	
	2023	1.46	18.10	56.94	8.25	0.00	
S4	2021	2.41	10.38	32.40	2.63	0.00	Predominantly coarse sediments across the entire reach.
	2022	1.92	16.16	44.26	2.62	0.00	
	2023	1.91	25.06	52.43	2.74	0.00	
S3	2021	0.66	22.47	104.71	1.19	0.00	Heterogeneous: coarser material mainly upstream, with progressive downstream fining.
	2022	0.70	20.49	105.79	1.25	0.00	
	2023	0.72	40.68	103.41	1.27	0.00	
S2noveg	2021	4.36	17.04	72.61	2.05	0.16	Heterogeneous: coarser material mainly upstream, with progressive downstream fining.
	2022	4.50	14.35	71.57	2.05	0.73	
	2023	4.41	20.00	70.20	2.07	2.87	
S2veg	2021	4.79	18.55	40.42	0.96	36.26	Heterogeneous: coarser material mainly upstream, with progressive downstream fining.
	2022	4.27	20.01	47.02	0.90	35.24	
	2023	4.31	19.53	44.15	0.93	38.95	
S1	2021	1.01	17.26	54.71	7.30	38.11	Strongly heterogeneous: coarse material upstream with progressive downstream fining.
	2022	0.94	16.77	53.20	7.38	39.18	
	2023	0.97	19.83	48.44	7.41	42.68	

resolution photogrammetric data from 2021 to 2023. Key geomorphic variables, including slope and Active Channel Width (ACW), were measured to assess their influence on the *BRI** and to compare proglacial contexts with previous observations. The following sections detail the case study and the methods used for data acquisition, processing and analysis.

3.1. Data acquisition and photogrammetric products

This study employs a morphometric analysis based on the calculation of the *BRI** from high-resolution Digital Surface Models (DSMs). Our monitoring activities on the Rutor proglacial area started in 2021, with annual data collection at the end of each hydrological year. Each year, following the hydrological cycle, aerial photogrammetric surveys were conducted over the glacier (since 2020) and proglacial area (since 2021) by Digisky, a specialized geomatics company. These surveys were carried out using crewed photogrammetric flights, which provided high-resolution data critical for analyzing the dynamic environment of the proglacial area. The photogrammetric flights were conducted in the early morning, coinciding with the period of minimum daily discharge, which is well-suited for calculating *BRI** and comparing it in space and time. Fig. 2 illustrates the water discharge time series at the outflow of

S2 during the photogrammetric flight acquisitions.

The photogrammetric datasets were processed to generate orthophotos and DSMs, achieving a high planimetric resolution ranging from about 0.1 to 0.2 m (Table 2; see Supporting Information S1 for details on data acquisition and processing). This high resolution was essential for capturing the fine-scale morphodynamics of the fluvial systems and allowed for detailed spatial analysis. To ensure a consistent 3D reference system across years, each UAV-SfM survey was georeferenced using a network of ground control points (GCPs) and independent check points (CPs) measured in the field, and processed through a bundle adjustment; the resulting orthophotos and DSMs were then co-registered and quality-checked using the CP residuals/accuracy metrics to guarantee inter-annual comparability of elevation and planimetric products (Corte et al., 2024).

3.2. Topographic metrics and statistical analyses

The classification of water bodies, dry areas, and vegetated zones was performed through manual photo-interpretation of the orthophotos. Although the automation of such tasks is common in geomatic applications (Le Men et al., 2002; Tetteh and Schönert, 2015), this process required a manual approach due to the variability in water color across different sections of the fluvial systems. In fact, the proglacial environment is characterized by a high degree of heterogeneity and the Rutor proglacial area's water bodies display a wide range of color shades due to variations in suspended sediment concentration. This variability made it difficult to apply automated classification algorithms reliably, necessitating manual delineation to ensure the accuracy of the resulting masks. Despite the labour-intensive nature of this process, it was essential for maintaining the integrity of the subsequent morphometric analyses.

For each fluvial system, cross-sections were generated along the flow

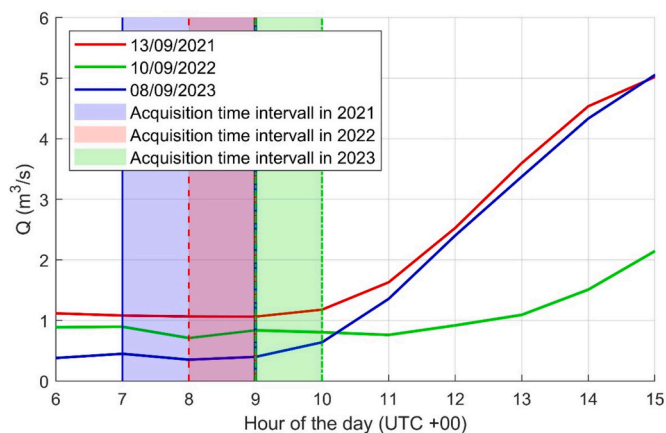


Fig. 2. Water discharge measured at the outflow of S2 during the photogrammetric flight acquisitions.

Table 2

Photogrammetric flights over the Rutor proglacial (2021–2023). The table reports the number of ground control points (GCPs) and check points (CPs), and the orthophoto and DSM ground sampling distance (cm/pixel).

Date of acquisition	n. of GCPs	n. of CPs	Orthophoto Resolution (cm/pix)	DSM Resolution (cm/pix)
13/09/2021	9	4	6.3	12.5
10/09/2022	10	6	7.0	14.9
08/09/2023	8	8	10.0	17.9

direction at regular 1 m intervals. Within each cross-section, data points were spaced at 0.2 m intervals to capture fine-scale variations in channel morphology. The planform geometry of the cross-sections was adapted to reflect the dominant morphological pattern of each system. In systems such as S4 and S2noveg, where the channel develops predominantly in a single direction, straight cross-sections were employed. Conversely, for systems exhibiting a delta-shaped planform, curvilinear cross-sections in the form of arcs of concentric circles were used. An example of the applied cross-section layout is shown in Fig. 3, which illustrates the ACW boundary, the internal division between S2veg and S2noveg, and the spatial distribution of cross-sections across both sectors.

For each cross-section, several parameters were calculated, including ACW, water width (WW), vegetated area percentage, number of channels (NC), BRI^* , and slope (S). The delineation of the ACW's boundary was performed using a combination of orthophotos and high-resolution DSMs. In particular, in areas where the system was bordered by vegetated banks, bedrock, or moraines, the delineation was guided by orthophotos. Whereas in the absence of these features, the boundaries were determined using DSM data, following slope lines to define the limits of morphodynamically active zones.

The ACW for each cross-section was determined by measuring the distance along the cross-section between the first and last points within the boundary, excluding segments covered by vegetation (Toone et al., 2014; Belletti et al., 2015). The BRI^* was calculated following the methodology outlined by Liébault et al. (2013) where the index is defined as the ratio between the standard deviation of elevations along the cross-section and the ACW:

$$BRI^* = \frac{1}{ACW} \cdot \sqrt{\frac{1}{n-1} \cdot \sum_{i=1}^n (z_i - Z)^2} \quad (1)$$

where z_i is the elevation of the i -th point of the cross-section, consisting of n equidistant points; Z is the mean elevation of the cross-section; and ACW is the active channel width (Fig. 4).

Due to the nature of the geomatics acquisition techniques, bathymetric data were not collected, so the elevation points used for BRI^* calculations correspond exclusively to the dry portions of the cross-sections. Surveys were conducted during low-flow conditions and to evaluate the potential impact of discharge variations—and consequently the elevation of the lowest points within the dry areas—between the three survey dates on BRI^* values, we analyzed continuous water level data recorded at the outflow of S2 in 2021 and 2022. Although data for 2023 were unavailable, we found a water level difference of approximately 0.11 m between 2021 and 2022 during the photogrammetric

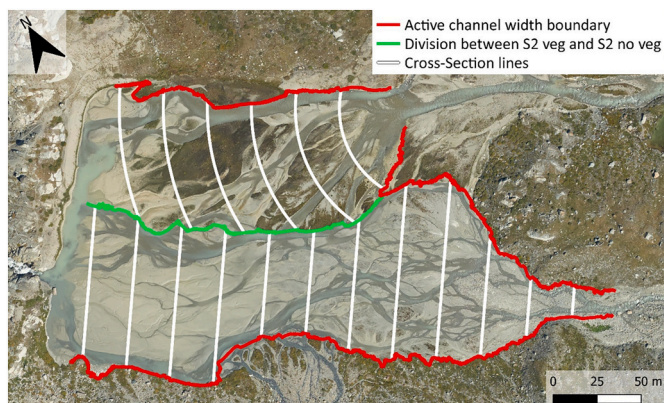


Fig. 3. Orthophoto of the S2 system in 2023 showing the delineation of active channel width boundaries and the internal division between S2veg (top) and S2noveg (bottom). White lines represent a subset of the cross-sections used in the analyses, spaced at 25 m intervals. For visualization purposes, not all cross-sections are shown.

flights. This difference is minimal compared to the average annual cross-sectional elevation variation within S2, which is around 0.76 m. These findings suggest that discharge-related uncertainties between survey dates are unlikely to significantly impact BRI^* comparisons across years.

Terrier et al. (2019) set a regional BRI^* threshold of 0.004, as derived from Liébault et al. (2013). Reaches with BRI^* values below this threshold are considered transport-limited, exhibiting a braided pattern indicative of abundant sediment supply, while BRI^* values above 0.004 suggest the reach is sediment-supply limited.

Slope was computed from the longitudinal elevation profile using a moving-window approach: for a target window length L_w , the local slope at each cross-section was estimated from the elevation difference between two profile points located approximately $\pm L_w/2$ upstream and downstream; near the reach limits, the window is truncated to remain within the mapped extent, so the effective distance decreases progressively toward the ends. A common guideline is to extract channel slope over a reach length of ~ 10 – 15 times channel width (e.g., Pitlick et al., 2008; Gob et al., 2025). In our case, the mapped proglacial reaches are short (Table 1; elongation values), so a 10 – $15 \times$ width window would often be comparable to, or exceed, the available reach length, reducing its applicability and limiting the ability to resolve along-reach variability. We therefore retained a fixed minimum window length of $L_w = 18$ m, chosen to be applicable to all reaches, as it is equal to 50% of the shortest mapped reach, 36 m. A Principal Component Analysis (PCA) was conducted to investigate the relationships among morphological and environmental variables describing the systems. PCA is a statistical method that reduces the dimensionality of a dataset while retaining as much variance as possible by transforming the original variables into new, uncorrelated variables called Principal Components (PC). Each PC is a linear combination of the original variables and represents a distinct pattern of variability within the data. The analysis, performed using the PCA function of MATLAB included data from all cross-sections of the studied proglacial systems. The variables analyzed included S, BRI^* , WW, ACW, and NC.

In addition to the exploratory PCA, we quantified the main bivariate controls highlighted in the results by fitting power-law relationships between BRI^* and ACW, and an exponential relationship between BRI^* and slope. For the ACW– BRI^* scaling, we also evaluated the published power-law fit of Liébault et al. (2013) against our dataset by computing predicted BRI^* values and summarizing the mismatch with a root-mean-square error (RMSE) and an R^2 calculated against the observed values.

Because PCA and bivariate fits indicate that BRI^* covaries with both slope and ACW, we subsequently used a multiple linear regression in log-space to quantify and remove their joint influence, yielding a combined normalized metric derived from the regression residuals. Specifically, we fitted the following log-space multiple linear regression model:

$$\log(BRI^*) = \alpha + \beta_S \cdot \log(S) + \beta_{ACW} \cdot \log(ACW) \quad (2)$$

where S is slope (dimensionless) and ACW is active-channel width (m). The model was fitted using ordinary least squares (MATLAB fitlm). A combined normalized metric was then derived from the residuals:

$$BRI_{S-ACW}^* = \frac{BRI^*}{S^{\beta_S} \cdot ACW^{\beta_{ACW}}} \quad (3)$$

The regression analysis was performed by including data points from all cross-sections of all systems, for a total of 2808 points, ensuring a robust dataset.

4. Results

4.1. Analysis of reach-scale BRI^* values

The analysis of BRI^* across the different multi-channel systems reveals significant inter-site variability (Table 3, Fig. 5). S1 consistently

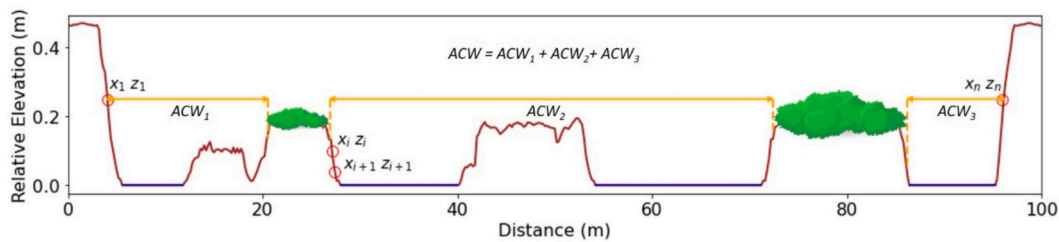


Fig. 4. Schematic representation of the calculation of the Bed Relief Index (BRI^*) based on the methodology of Liébault et al. (2013). The figure illustrates a cross-section of a fluvial system, showing the Active Channel Width (ACW) components (ACW_1 , ACW_2 , ACW_3) and the relative elevation of the channel bed points (z_i). The blue line represents the water surface, with its elevation set to zero in this representation for simplicity.

Table 3

Mean BRI^* (\pm standard deviation) for all multi-channel systems in time.

System	2021 (mean \pm SD)	2022 (mean \pm SD)	2023 (mean \pm SD)
S1	0.0085 \pm 0.0114	0.0081 \pm 0.0104	0.0082 \pm 0.0096
S2 veg	0.0023 \pm 0.0014	0.0017 \pm 0.0005	0.0019 \pm 0.0005
S2noveg	0.0021 \pm 0.0034	0.0022 \pm 0.0025	0.0019 \pm 0.0022
S3	0.0014 \pm 0.0012	0.0014 \pm 0.0009	0.0016 \pm 0.0010
S4	0.0038 \pm 0.0023	0.0039 \pm 0.0030	0.0064 \pm 0.0050
S5	0.0059 \pm 0.0047	0.0061 \pm 0.0040	0.0044 \pm 0.0022
S6	0.0052 \pm 0.0078	0.0055 \pm 0.0084	0.0060 \pm 0.0095

exhibit BRI^* values well above the 0.004 threshold across all years considered (2021–2023), potentially indicating a sediment-supply-limited regime. Reaches S5 and S6 also display BRI^* values above the threshold, although being closer to it—particularly in 2023 for S5—suggesting sediment-supply-limited conditions, albeit less markedly than in S1. In contrast, S2 and S3 consistently remain below the threshold, indicating a transport-limited regime characterized by abundant sediment availability. S4 lies close to the threshold, remaining slightly below it in 2021–2022 and exceeding it in 2023.

Temporal analysis from 2021 to 2023 acquisitions reveals a general stability in BRI^* values across most systems, with the exception of S5, which shows a significant decrease in 2023 (Fig. 5). This change in S5 is accompanied by an increase in both the length and ACW of the upstream delta, suggesting an evolving sediment transport dynamic.

S6 exhibits an increase in BRI^* values over time, suggesting increasing sediment-supply limitation in this area.

4.2. Analysis of the cross-section data

The results, presented in Fig. 6, include a Pareto plot that illustrates the proportion of variance explained by each PC, helping to assess the importance of each principal component. The biplot is also provided, showing the distribution of the first two principal components, which visually represents how the original variables contribute to the principal components and how cross-sections or systems are distributed in the reduced-dimensionality space.

The PCA (Fig. 6a) indicates that significant correlations exist between variables, since the first and second components explain respectively 56% and 23% of the variance. This suggests that BRI^* is not independent of other geomorphic variables such as slope, ACW, and the NC, and thus for inter-site comparisons with contrasted slope and ACW, it is necessary to remove such effects. In the PCA plot (Fig. 6b), BRI^* and slope are correlated, appearing in the same quadrant, while the other variables cluster together in the opposite direction, indicating their interrelated nature.

BRI^* is in fact connected to WW , NC , and ACW through power law relationships. The Pearson correlation analysis, adopted by using the logarithms of the values from each cross-section, results in p -values much smaller than 0.001, indicating a highly statistically significant relationship. The negative correlation coefficients obtained show an inverse relationship between BRI^* and the three variables— WW , NC , and ACW . Thus with larger values the BRI^* value tends to be smaller.

The scatter plot in Fig. 7 illustrates the relationship between ACW and the BRI^* across the Rutor proglacial systems. The inverse correlation is highlighted by the power law fit to the observed data, which is expressed as:

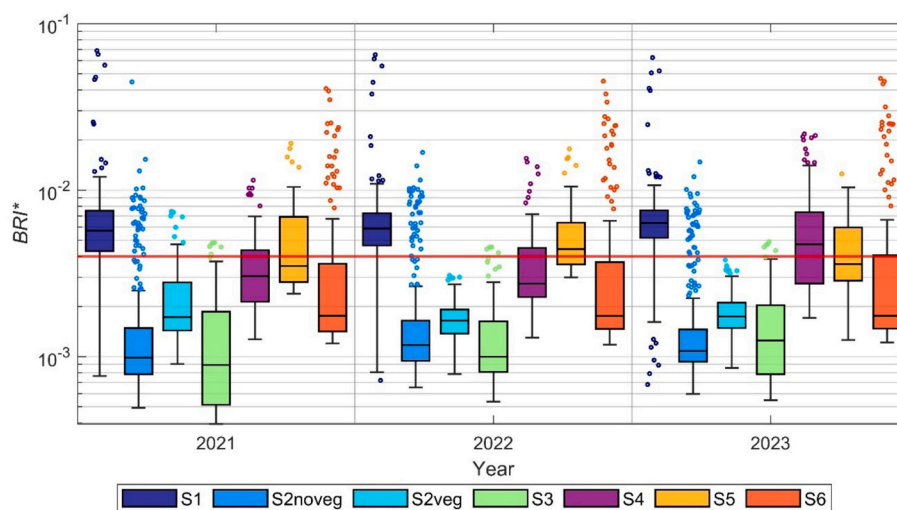


Fig. 5. Box plots displaying the BRI^* metrics for each system across three years. The left panel illustrates the average BRI^* values for each system. The right panel shows the distribution of BRI^* values across all Cross-Sections (C-Ss) within each system, with the y-axis presented in logarithmic scale.

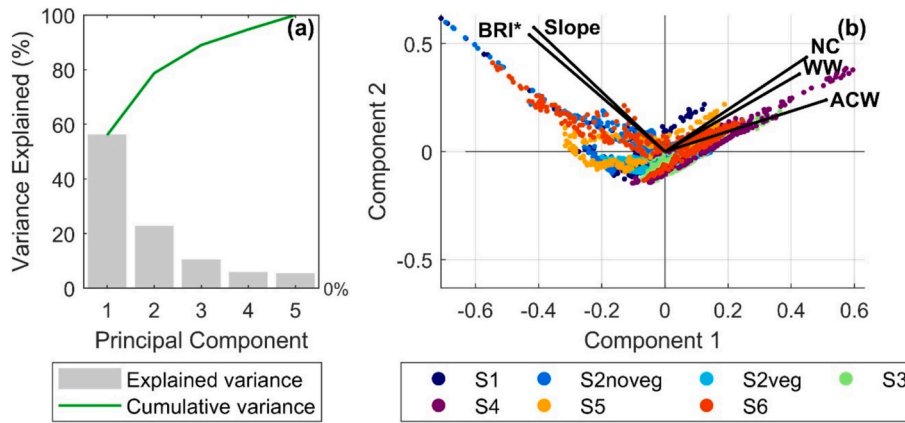


Fig. 6. Principal Component Analysis (PCA) results for cross-sections of Rutor proglacial systems: (a) Pareto plot showing the percentage of variance explained by each Principal Component (PC); (b) PCA biplot illustrating the distribution of the first two PCs. Key contributing variables include slope, BRI^* , WW (Water Width), ACW (Active Channel Width), and NC (Number of channels). Different colors represent distinct systems.

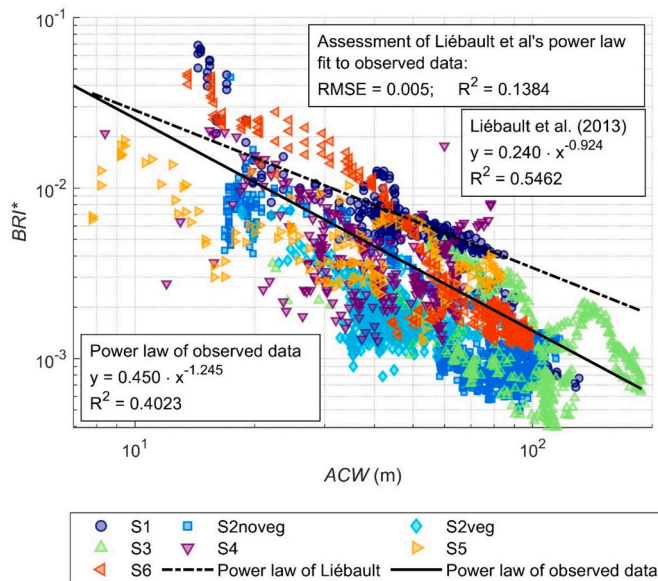


Fig. 7. Scatter plot of active channel width versus BRI^* for cross-sections of the studied fluvial systems. Both axes are presented on a logarithmic scale. The black solid line represents the power law fit for the observed dataset, while the black dash-dot line corresponds to the power law from Liébault et al. (2013) applied to its original dataset. The annotation boxes summarize the corresponding equations and goodness-of-fit metrics, including the assessment of Liébault et al.'s power law when applied to the present data.

$$BRI^* = 0.450 \cdot ACW^{-1.245} \quad (4)$$

with an R^2 value of 0.40, indicating moderate explanatory power of the model. This shows that wider channels tend to have lower variability in the bed relief, as represented by the BRI^* . The power law derived from the observed data differs from the one derived from the data of Liébault et al. (2013), where

$$BRI^* = 0.240 \cdot ACW^{-0.924} \quad (5)$$

with a higher R^2 value of 0.55, indicating a stronger fit to their dataset.

Following the analysis of ACW , we next examined the relationship between slope and BRI^* to explore additional geomorphic controls on bed roughness. The resulting exponential fit, presented in Fig. 8, demonstrates a significant relationship with an exponent of 13.41 and an R^2 value of 0.57. The relatively modest R^2 value indicates that, while there

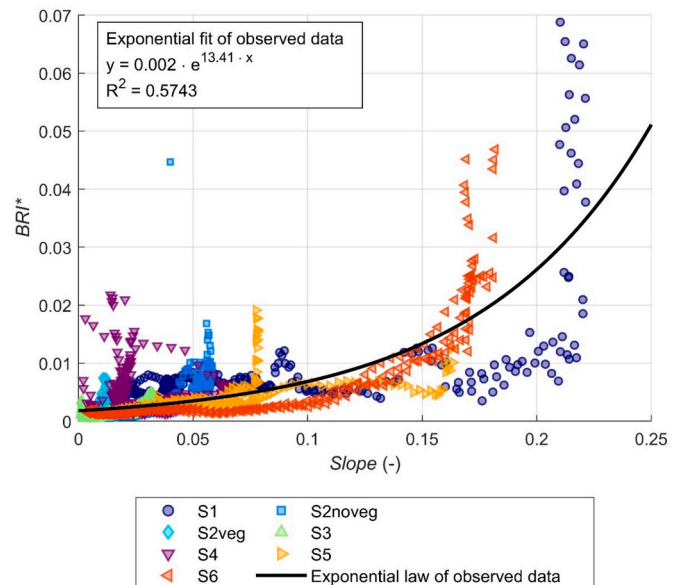


Fig. 8. Scatter plot of BRI^* versus slope across different systems. The black line represents the exponential fit of the observed data, with the corresponding equation and coefficient of determination shown in the box.

is a detectable correlation between BRI^* and slope, slope alone accounts for only a portion of the variability in BRI^* , which aligns with the findings from the PCA. The exponential relationship suggests that BRI^* increases with slope in a nonlinear manner, with BRI^* values rising sharply at higher slopes. This nonlinear trend implies that while slope is an important driver of sediment dynamics, additional local factors likely influence BRI^* values, leading to the observed variability within reaches that have similar slopes but different BRI^* values. This variability highlights the complex interplay of geomorphic and environmental factors beyond slope, which modulate the BRI^* response within the systems.

4.3. Longitudinal variability of BRI^*

The longitudinal analysis of BRI^* across the six proglacial multi-channel systems (Fig. 9) reveals distinct patterns in geomorphic characteristics. For most systems (S1, S2noveg, S5, and S6), BRI^* values generally decrease from upstream to downstream, mirroring the downstream reduction in slope. In these systems, ACW and the NC both

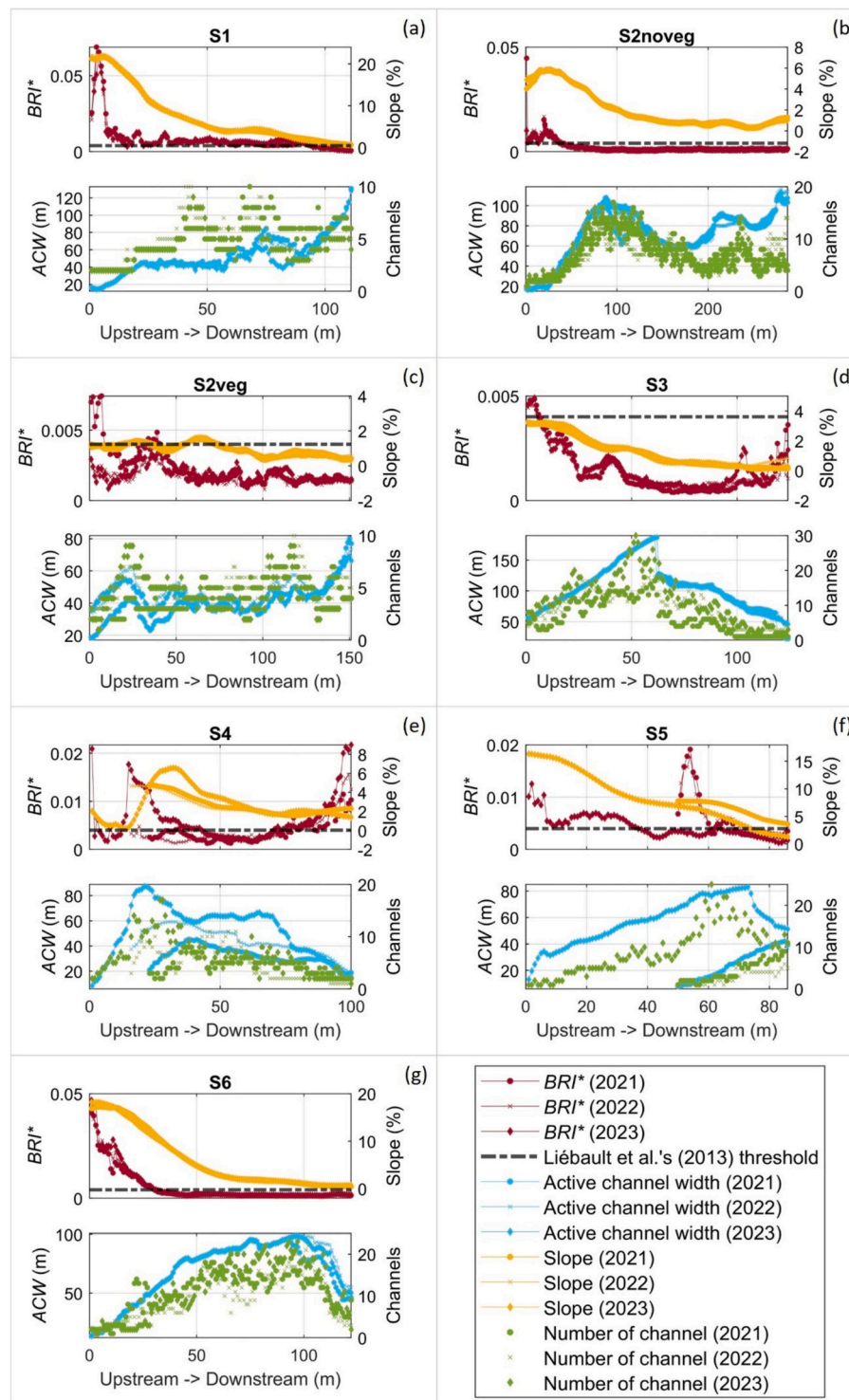


Fig. 9. Longitudinal variation of BRI^* (red) and slope (orange) in the top graph, and active channel width (blue) and number of channels (green) in the lower graph for S1 (a), S2noveg (b), S2veg (c), S3 (d), S4 (e), S5 (f), and S6 (g) in 2021 (dot), 2022 (x), and 2023 (diamond).

increase progressively downstream. The apparent downstream decrease observed in the most downstream cross-sections is due to the increasing proportion of each section that falls within the lake area, which is not considered part of the active channel. As a result, channel segments located within the lake are excluded from the analysis of ACW and channel count. In contrast, the reach S4 exhibits a unique trend with BRI^* increasing downstream, differently from the pattern observed in the deltas. The ACW and the NC in S4 are relatively low both at the upstream and downstream ends of the reach, but they display a

pronounced increase in the middle section of the reach. S2veg displays relatively stable BRI^* values along their lengths, which remain mostly below the threshold of 0.004. This contrasts with S1, S2noveg, S3, S5, and S6, where BRI^* values exceed the 0.004 threshold in upstream segments before decreasing below it downstream. In S4, the trend is reversed: BRI^* values are below the 0.004 threshold upstream and exceed it downstream.

Overall, most deltas exhibit broadly consistent trends in decreasing BRI^* and slope, paired with increasing ACW and NC from upstream to

downstream, while the braided reach S4 stands out with its increasing BRI^* downstream.

4.4. Multiple regression analysis of BRI^* with slope and ACW

We performed a multiple regression analysis to explain the variability in $\log(BRI^*)$ using $\log(S)$ and $\log(ACW)$ as explanatory variables. The decision to include both parameters is due to their strong influence that we observed on BRI^* . The fitting model results in:

$$\log(BRI^*) = -0.938 + 0.426 \cdot \log(S) - 0.861 \cdot \log(ACW) \quad (6)$$

The coefficient for $\log(S)$ is 0.426, indicating a positive effect on $\log(BRI^*)$. This suggests that as slope increases also BRI^* tends to increase. In contrast, $\log(ACW)$ has an exponent of -0.861 , which indicates a negative effect on $\log(BRI^*)$. This implies that larger ACWs are associated with lower values of BRI^* . The coefficients for $\log(S)$ and $\log(ACW)$ were found to be statistically significant ($p < 0.001$) based on the t -tests from the multiple linear regression model, confirming that slope and ACW are critical factors influencing BRI^* . The model has an R^2 value of 0.759, meaning that approximately 75.9% of the variance in $\log(BRI^*)$ is explained by the combined effects of log-transformed slope and ACW.

Given the influence of both slope and ACW on BRI^* , we sought to create a normalized version of BRI^* that is independent of these two parameters. By adjusting for the effects of slope and ACW, the normalized parameter would allow us to classify systems in the Rutor proglacial area in a way that is less affected by differences in these two explanatory variables. This normalized BRI^* parameter, which we denote as BRI^*_{S-ACW} , is calculated as follows:

$$BRI^*_{S-ACW} = \frac{BRI^*}{Slope^{0.426} \cdot ACW^{-0.861}} = \frac{\sqrt{\frac{1}{n-1} \cdot \sum_{i=1}^n (z_i - Z)^2}}{Slope^{0.426} \cdot ACW^{0.139}} \quad (7)$$

Fig. 10 illustrates the relationship between BRI^*_{S-ACW} and slope (panel a) and ACW (panel b) for all systems in all years.

5. Discussion

5.1. Geomorphic heterogeneity and transitional morphologies

A closer examination of the individual systems reveals that several reaches do not conform to a single morphological type but they instead exhibit transitional features that evolve over time or vary spatially within the same system. For example, S1 can be interpreted as a fan-delta formation, based on its slope, configuration and the diverging distributary network that lacks rejoining channels. Fan-deltas form

where alluvial fans prograde directly into standing bodies of water and are characterized by debris-flow deposits and poorly developed distributary systems (Galloway, 1991; Patranabis-Deb and Chaudhuri, 2007).

S2 presents an even more nuanced case, as it comprises two distinct sectors: S2veg and S2noveg. Possibly due to vegetation differences, these two areas differ in channel organization. The S2veg sector shows a radial arrangement of distributary channels that diverge outward from a single origin without reconnections, a characteristic consistent with fan-delta systems. In contrast, S2noveg is fed by a braided upstream channel network and displays a more longitudinal channel alignment, which supports its classification as a braided-delta.

S3 further illustrates this special transitional behavior. In 2021, the northeastern portion of the delta exhibited a configuration resembling braided systems, where the number of bifurcations was approximately equal to the number of convergences—a pattern that contrasts with the classic deltaic morphology, typically dominated by bifurcations.

Similarly, the morphological classification of S5 varies across the study period. In 2021, the system maintained a simple deltaic structure. In 2022, the emergence of multiple non-rejoining distributary channels justified its reclassification as a fan-delta. By 2023, the system exhibited substantial complexity: the upper reach, characterized by a steep gradient, diverging non-rejoining channels and coarser surface texture, was interpreted as a fan; the middle western section displayed features typical of braided systems with a more mixed surface texture; the downstream portion retained its deltaic identity with a developed distributary systems and a relative fining toward the lake margin (Fig. 11).

Finally, in 2023, the northwestern part of S6 showed clear morphological indicators of braiding, such as interconnected multi-thread channels, leading to its classification as partially braided, while the remaining area continued to function as a delta. Notably, the deltaic sector also exhibits several zones of apparent subsurface flow, where wetted channels emerge directly from bars in the orthophotos, highlighting locally complex surface–subsurface connectivity.

These observations reinforce the notion that reach-scale classifications should be considered as flexible and context-dependent, particularly in rapidly evolving proglacial environments.

Fig. 12 shows the distribution of BRI^* values of sections across different geomorphological system types—braided (B), delta (D), and fan/fan-delta (F)—for each year from 2021 to 2023. This classification reflects the internal geomorphic heterogeneity of the systems, as described in the paragraphs above, and accounts for portions within the systems assigned to different categories. Fan systems—including S1, S2 veg, S5 in 2022, and the fan-classified portions of S5 in 2023—consistently show the highest mean BRI^* values, all above the threshold. Braided systems—which include S4 and the braided portions of

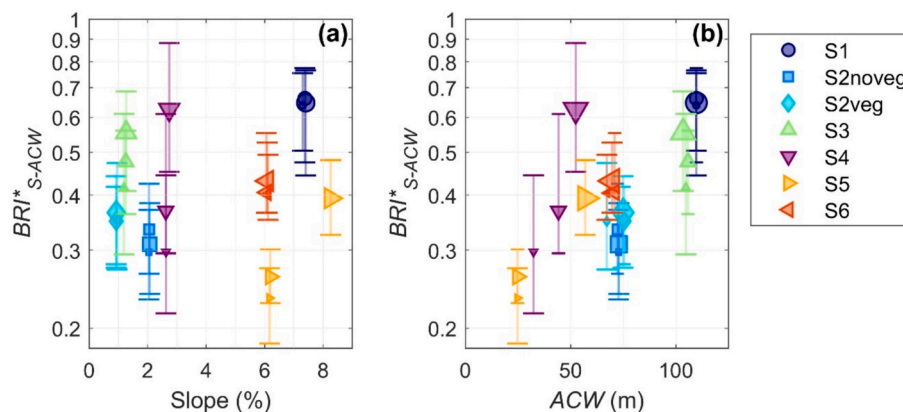


Fig. 10. Scatter plots showing the relationship between the median BRI^*_{S-ACW} and the average slope (a) and ACW (b) for the different plot systems from 2021 to 2023. Each system is represented by distinct colors and shapes, with the size of the markers indicating the year (smallest for 2021, medium for 2022 and largest for 2023). Vertical lines span from the 25th to the 75th percentile for each system-year dataset, terminated by short horizontal bars.

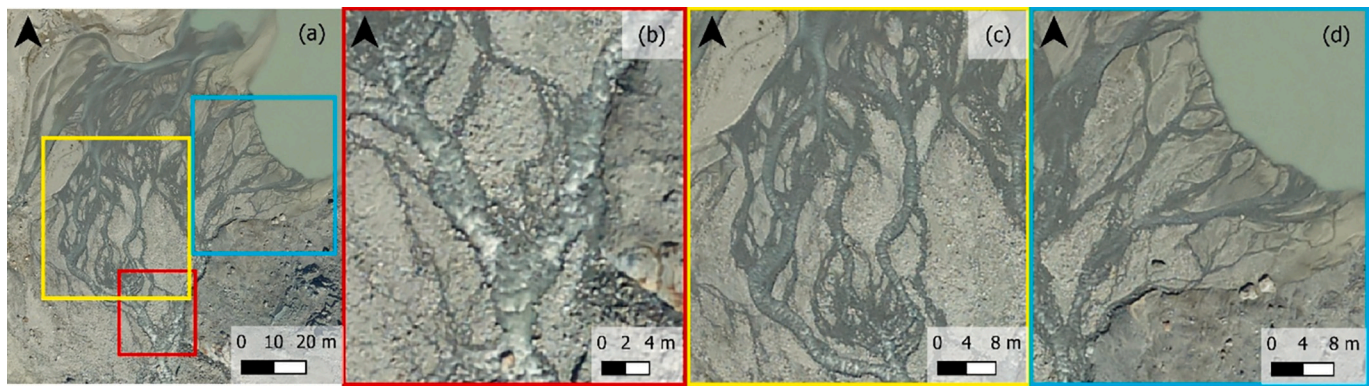


Fig. 11. Orthophoto-based example of within-reach geomorphic heterogeneity in S5 (2023). (a) Reach overview showing the locations of the zoomed panels. (b) Upstream fan-like sector, (c) intermediate braided sector, and (d) downstream deltaic sector at the lake margin.

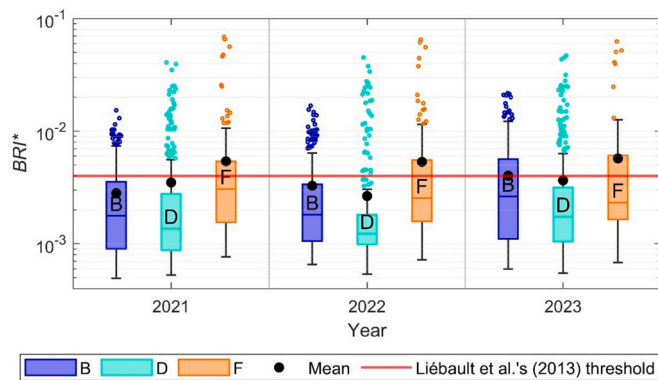


Fig. 12. Box plots displaying the BRI^* metrics for each system type (B = braided, D = delta, F = fan/fan-delta) across three years with the y-axis presented in logarithmic scale.

S2noveg, S3 in 2021, S5 in 2023, and S6 in 2023 — also exhibit mean BRI^* values above the threshold in most years, though with slightly lower medians and means than fan systems. Deltaic systems — including the downstream end of S2noveg, S3 (excluding the braided portion in 2021), S5 in 2021, S6 in 2021 and 2022, and the delta-classified portions of S5 and S6 in 2023 — generally exhibit mean BRI^* values below the threshold.

The Kruskal–Wallis tests (Kruskal and Wallis, 1952) revealed significant differences in BRI^* among all three geomorphological system types, with post-hoc analysis (Šidák, 1967) confirming that each pair (B–F, B–D, F–D) differed significantly both in the overall dataset and in each individual year (2021, 2022, and 2023; Table 4).

These results underscore the internal morphological complexity of proglacial systems, where deltaic reaches often contain segments that exhibit fan-like or braided characteristics to varying degrees. Rather

Table 4

Results of Kruskal–Wallis tests comparing BRI^* among geomorphological system types (B = braided, D = delta, F = fan/fan-delta) for the overall dataset and for each year (2021–2023). The table reports the Kruskal–Wallis H statistic and associated p -value, and post-hoc pairwise comparisons (Dunn test) with Šidák-adjusted p -values (padj).

Period	Kruskal–Wallis		Post-hoc (Dunn–Šidák padj)		
	H Statistic	p-value	B vs F	B vs D	F vs D
Overall	254.31	<0.001	<0.001	<0.001	<0.001
2021	96.26	<0.001	<0.001	0.152	<0.001
2022	139.35	<0.001	<0.001	<0.001	<0.001
2023	49.13	<0.001	0.004	<0.001	<0.001

than representing strictly distinct categories, the classification serves to capture the dominant features within systems that may undergo morphological transformations during their development or over time.

All the studied systems are multithreaded but shaped by different hydro-sedimentary drivers. Deltas have a lower BRI^* as they are constrained by a base-flow. If BRI^* significantly changed in such context, it would indicate a change in the downstream base level imposed by the lake, which is not observed in the present study. Fan and braided-channel BRI^* values are primarily controlled by upstream conditions rather than by base-level, and their morphology can adjust to variations in sediment supply.

5.2. Reanalyses of BRI^* after removal of ACW and slope effects

Our findings highlight the interactions among geomorphic variables that influence BRI^* in proglacial systems. PCA and Pearson correlation analyses reveal that BRI^* is closely associated with factors such as slope and ACW, which recall the underlying geomorphological processes. To remove the joint influence of slope and active-channel width on BRI^* , we rely on the combined normalization BRI^*_{S-ACW} . Compared to the first-order classification based on raw BRI^* (using the Terrier et al., 2019 threshold), the relative ordering given by BRI^*_{S-ACW} differs for some systems. Notably, S5 shifts toward the highest BRI^*_{S-ACW} values in 2021–2022, whereas S3 no longer appears among the most sediment-rich systems inferred from BRI^* and instead plots in an intermediate position once slope and width are accounted for. In the following, we use reach-scale summaries of BRI^*_{S-ACW} to interpret the contrasting behavior of individual systems and their temporal trajectories.

S6 is fed by a confined, single-thread stream draining the left glacier tongue. Proximal proglacial channels commonly remain entrenched and high-energy where confinement promotes a single-thread course (Maizels, 2002); incision is frequently reported immediately downstream of glacier outlets when transport capacity exceeds bedload supply (Carrivick and Heckmann, 2017; Mancini et al., 2024). In addition, the presence of an upstream proglacial lake introduces a strong connectivity break between the ice margin and the fluvial reach: proglacial lakes can buffer meltwater discharge dynamics and act as effective sediment traps, capturing a substantial fraction of sediment that would otherwise be transferred downstream. (Carrivick and Heckmann, 2017; Delaney et al., 2018). The intermediate BRI^*_{S-ACW} levels observed in S6 are consistent with this mixed setting, where downstream sediment conditions may reflect both reduced upstream supply and local contributions released by channel incision and pattern adjustment when bedload supply is low (Delaney et al., 2018; Mancini et al., 2024).

S5 shows the lowest reach-scale BRI^*_{S-ACW} values in 2021–2022, but a marked increase in 2023, while still remaining intermediate within the Rutor forefield. This temporal shift coincides with a clear reorganization of the feeder network at the glacier margin, where multiple incised

channels contribute meltwater in 2021–2022, whereas in 2023 flow becomes more focused into fewer pathways, with abandonment of one branch and widening of a dominant channel. Such rapid channel activation/deactivation and short-lived flow paths, together with widening of the active channel prior to abandonment or further rerouting, are consistent with documented patterns of proglacial drainage self-reorganization during glacier retreat (Savi et al., 2024). In proglacial forefields, concentrating discharge into fewer channels is expected when transport capacity becomes relatively higher than upstream sediment supply, because hydraulically efficient single thread configurations tend to reinforce the erosional tendency and modify sediment export (Mancini et al., 2024). Accordingly, the increase in BRI^*_{S-ACW} in 2023 may indicate that S5 shifted toward more supply-limited conditions, plausibly due to a stronger focusing of meltwater into the reach without a proportional increase in bedload input, and/or a progressive depletion/armouring of readily erodible sediment as erosion concentrates along the dominant pathway. This interpretation is consistent with experimental–numerical evidence that reduced bedload supply can rapidly drive a transition toward less morphodynamically intense states and confined-channel configurations (Mancini et al., 2025).

S4 is the reach closest to the glacier front and is directly fed by meltwater from the right tongue. In many proglacial settings, the immediate downstream channel is expected to be entrenched and commonly single-thread where transport capacity exceeds sediment supply, producing incision near the ice margin (Mancini et al., 2024). In S4, however, we observe a braided pattern, which suggests that sediment availability at the outlet is high enough for supply to match or exceed transport capacity, promoting aggradation and multithread channel development even in proximal positions (Maizels, 2002; Mancini et al., 2024). This interpretation is consistent with the combined normalization, as reach-scale BRI^*_{S-ACW} values for S4 are among the lowest in 2021–2022. Despite its overall braided planform, S4 shows a marked longitudinal organization of bed relief: BRI^* increases downstream along the reach (Fig. 9), with the highest values concentrated in the downstream sector. A plausible interpretation is that local boundary conditions downstream S4 impose a steeper, more confined single-thread segment that promotes bed destabilization and incision during high-melt events. Under this scenario, incision initiated downstream can propagate upstream (regressive erosion), producing higher bed relief in the downstream sector. S3 is fed by a single-thread reach connecting downstream of S4, and the terminal portion of this feeder channel displays a step-pool morphology. Step-pool reaches are commonly associated with steep, high-energy conditions where transport capacity can exceed sediment supply, so supply-limited behavior may be more likely than in lower-gradient alluvial morphologies (Montgomery and Buffington, 1997). In addition, step-pool sequences can promote localized sediment storage within pools and an episodic release of stored material, which may make sediment delivery to downstream reaches more discontinuous (Montgomery and Buffington, 1997). Taken together, these mechanisms provide a plausible explanation for the intermediate BRI^*_{S-ACW} values observed in S3, which may reflect a downstream reach that is not fully sediment-rich despite being connected to a proximal, sediment-abundant sector upstream.

S2 (S2veg and S2noveg) is classified as a proglacial outwash plain (sandur), i.e. a braided proglacial outwash surface formed under highly variable meltwater regimes. Sandar are typically sediment-rich, bedload-dominated environments with highly erodible bed and banks, and unconfined sandar are often dominated by aggradation while still undergoing frequent scour-and-fill and bar modification (Maizels, 2002; Carrivick and Russell, 2013). The consistently low reach-scale BRI^*_{S-ACW} values of both S2 sectors are most consistent with a transport-limited and aggrading behavior, where abundant, readily reworked outwash sediment promotes laterally distributed flow and comparatively smoother reach-scale bed relief for the given slope–width context. Both sectors are fed by lake-outlet streams from upstream proglacial lakes. While these lakes can trap part of the coarse load close to the ice margin,

downstream reaches commonly recover sediment availability by reworking readily mobilisable outwash deposits and channel/bank material, so that the flow arriving on the outwash plain can remain sediment-rich overall (Carrivick and Russell, 2013; Carrivick and Tweed, 2013). The slightly lower BRI^*_{S-ACW} values in S2noveg may reflect the steeper upstream channel that promotes more efficient downstream transport and local bed smoothing, whereas the vegetated sector may locally favour bar stabilisation and more spatially heterogeneous roughness (Lallias-Tacon et al., 2017); in both sectors, the values remain consistent with an outwash-plain setting dominated by abundant, reworkable sediment (Maizels, 2002; Carrivick and Russell, 2013).

S1 is the most distal reach in the proglacial sequence; under common proglacial sediment-budget patterns, erosion tends to dominate close to the ice margin whereas exported material preferentially accumulates in more distal sectors (Piermattei et al., 2023), which would typically promote higher downstream sediment availability—yet S1 shows among the highest BRI^*_{S-ACW} values. We interpret this as reduced effective sediment delivery to S1 relative to transport capacity, despite the large meltwater input. A key element is upstream storage associated with S2 and recurrent ephemeral ponding, which can interrupt sediment connectivity between the ice margin and downstream reaches (Carrivick and Tweed, 2013; Carrivick and Heckmann, 2017). Downstream of this upstream storage, the steep, incised, bedrock-influenced channel feeding S1 likely operates in a transport-dominated regime, where transport capacity can exceed the supply of mobile sediment. Such conditions are typical of steep mountain channels in which bedrock control and limited alluvial cover constrain sediment availability and downstream replenishment, consistent with the high BRI^*_{S-ACW} values observed in S1 (Montgomery and Buffington, 1997).

Over the three-year period, BRI^*_{S-ACW} values reveal diverse temporal patterns among the studied systems, with some maintaining consistent behaviors and others exhibiting notable trends of change (Fig. 10). S1 and S2 remain comparatively stable, suggesting that the balance between effective sediment supply and transport capacity did not change markedly over the study interval at the reach scale. In contrast, S3, S4, S5 and S6 display increasing BRI^*_{S-ACW} through time, indicating a shift toward rougher bed conditions and a relative decrease in sediment availability (or, equivalently, an increase in transport capacity relative to supply). For S3, this trend may reflect increasing control by the short single-thread connector reach with step-pool/cascade morphology, where coarse-bed organization and local storage/armouring can reduce downstream sediment delivery (Montgomery and Buffington, 1997). The increase in S4 BRI^*_{S-ACW} likely reflects increasingly asymmetric meltwater inputs as the glacier tongue retreats: discharge is delivered preferentially from one side, forcing channel activity to concentrate there, while reduced reworking on the hydraulic-right side favors the development of a small terrace. For S5, the sharp increase in 2023 is consistent with the reorganization of meltwater routing during glacier retreat—fewer, more concentrated feeder channels and the development/expansion of small proglacial ponds near the ice margin likely enhanced upstream deposition and reduced the effective sediment delivery to the reach. Finally, the progressive increase in S6 suggests an analogous tendency toward more supply-limited conditions, plausibly driven by growing upstream trapping as the lake expands and/or by declining local sediment release as the feeder channel incises and stabilizes.

Proglacial corridors can alternate between net erosion and net storage over short timescales, so downstream patterns of sediment availability are not necessarily monotonic (Delaney et al., 2024). In many Alpine forefields, erosion tends to dominate in the proximal zone (e.g., upstream of S5 and S6), while exported material preferentially accumulates in more distal sectors (e.g., S2); however, the magnitude and sign of storage depend strongly on local topography, confinement/accommodation space, and connectivity (Piermattei et al., 2023). Proglacial lakes and ponding commonly act as sediment sinks and can

decouple sediment transfer between the ice margin and downstream reaches (e.g., S1) (Carrivick and Heckmann, 2017).

5.3. Testing the applicability of BRI^* normalizations on external datasets

We extended our analysis to include external datasets in order to assess whether the proposed normalizations provide consistent classifications across different geographical and geomorphological contexts. Specifically, we utilized the dataset provided by Devreux et al. (2022), available on Zenodo (<https://zenodo.org/records/5796184>), which includes information from two distinct river systems: the Drac at Chabottes in 2018 and the Durance at Brillanne in 2017.

The Drac River, located in the French Alps, is characterized by sedimentary and metamorphic lithology and a nivo-pluvial hydrological regime. Devreux et al. (2022) analyzed a restored reach at Saint-Bonnet-en-Champsaur, where restoration occurred in 2013–2014, and a target reach at Chabottes. The restoration involved active channel widening and gravel augmentation to mitigate channel incision and restore braided morphology.

The Durance River, one of the largest braided river in southeastern France, flows through sedimentary and crystalline terrains and has a nivo-pluvial hydrological regime. Devreux et al. (2022) included data from a restored reach at La Brillanne and a target reach at Les Mées. Restoration at La Brillanne occurred later, between 2019 and 2021, so the dataset from 2017 represents conditions before the restoration took place. The restored reach had been previously impacted by extensive human interventions, such as flow regulation and sediment connectivity disruption. For each river, the available data comprised cross-sectional elevation, BRI^* , and ACW.

Durance river at Brillanne (2017) and Drac river at Chabottes (2018) have BRI^* values below the threshold of 0.004, suggesting that both are well supplied in sediment and transport-limited.

The boxplot comparisons in Fig. 13 highlight the patterns emerging from the external datasets when compared with the Rutor. The BRI^* distributions for the two external reference reaches are centred below (or close to) the 0.004 threshold, although several cross-sections exceed it and the BRI^* ranges partly overlap with the Rutor dataset (Fig. 13a). Once both slope and ACW effects are removed, BRI^*_{S-ACW} allows a more meaningful comparison across sites, distinguishing the Rutor from the external references.

The BRI^*_{S-ACW} results provide a coherent picture of site conditions:

- Durance at Brillanne, which is expected to be sediment-starved, displays the highest values, far above all other sites.
- Drac at Chabottes, which is a reference reach after restoration, results more sediment supplied than Durance at Brillanne but still less supplied than the Rutor.

- Rutor, expected to be the most sediment-fed, consistently exhibits the lowest values.

6. Conclusions

This study evaluated whether the Normalized Bed Relief Index (BRI^*) can inform on sediment-regime conditions in proglacial multi-channel systems, using multi-temporal high-resolution photogrammetric surface models from the Rutor Glacier forefield (Italian Alps). The results show that BRI^* provides a practical remote-sensing metric to characterize reach-scale macro-roughness and to distinguish contrasting morphodynamic states in rapidly evolving proglacial settings.

Across the dataset, BRI^* is not independent of other geomorphic controls: slope and active-channel width exert a strong and systematic influence on BRI^* . To enable more robust comparisons across reaches with different gradients and channel dimensions, we therefore implemented a combined normalization based on log-space multiple regression, producing a metric (BRI^*_{S-ACW}) that removes the joint effect of slope and active-channel width. This combined normalization improves cross-reach comparability and supports interpretation of sediment supply versus transport-capacity conditions across heterogeneous proglacial landforms.

Finally, applying the same normalization framework to independent braided-river datasets indicates that the combined normalization yields consistent discrimination among transport-regime conditions across different geomorphic contexts, supporting the broader applicability of the approach beyond the Rutor forefield. Overall, BRI^* —and especially its combined normalization—offers an efficient, repeatable indicator to monitor proglacial morphodynamic adjustment and sediment connectivity under changing boundary conditions, and motivates continued multi-temporal surveys to capture longer-term trajectories.

CRediT authorship contribution statement

E. Corte: Writing – original draft, Software, Methodology, Data curation. **M.M. Macelloni:** Data curation. **S. Tamea:** Writing – review & editing, Supervision, Investigation, Conceptualization. **C. Camporeale:** Writing – review & editing, Supervision, Investigation, Conceptualization. **H. Piégay:** Writing – review & editing, Supervision, Methodology, Conceptualization, Investigation.

Declaration of competing interest

The authors declare the following financial interests/personal relationships which may be considered as potential competing interests: Carlo Camporeale reports financial support was provided by Ministry of University and Research PRIN 2022. Carlo Camporeale reports financial

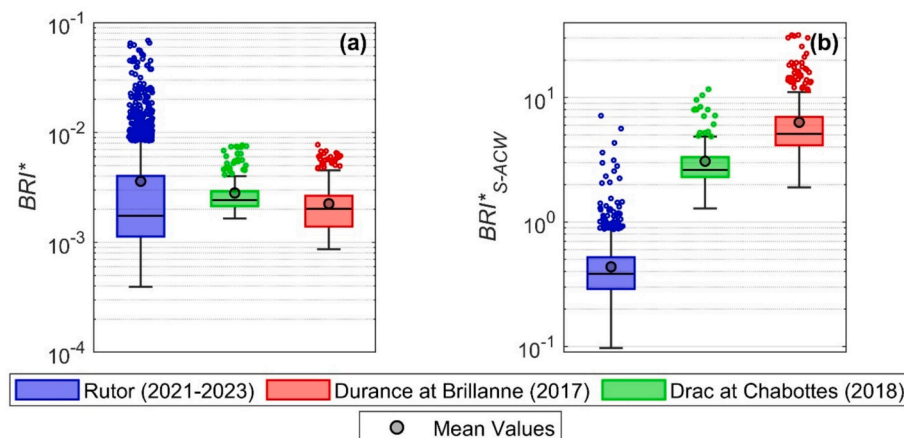


Fig. 13. Box plots comparing BRI^* and BRI^*_{S-ACW} for the Rutor dataset (2021–2023), Durance river at Brillanne (2017) and Drac river at Chabottes (2018).

support was provided by European Union (Horizon). Carlo Camporeale reports financial support was provided by Interreg ALCOTRA BECCA. Stefania Tamea reports financial support was provided by Interreg ALCOTRA BECCA. Elisabetta Corte reports financial support was provided by Interreg ALCOTRA BECCA. If there are other authors, they declare that they have no known competing financial interests or personal relationships that could have appeared to influence the work reported in this paper.

Acknowledgements

This study was carried out within the “Eco-geomorphic carbon pumping from rivers to blue carbon Ecosystems (e-Capture)” project, funded by the European Union – Next Generation EU within the PRIN 2022 program (D.D. 104 – 02/02/2022, Ministero dell'Università e della Ricerca), CUP E53D23004070006, and by the European Union (project Grant Agreement No. 101185000 — CONCERTO — HORIZON-CL5-2024-D1-01).

Views and opinions expressed are however those of the author(s) only and do not necessarily reflect those of the European Union or the European Climate, Infrastructure and Environment Executive Agency (CINEA). Neither the European Union nor the granting authority can be held responsible for them.

The authors also acknowledge the “Bacini Ecologicamente sostenibili e sicuri, concepiti per l'adattamento ai Cambiamenti Climatici (BECCA)” project, INTERREG VI-A France–Italy ALCOTRA 2021–2027, n. Synergie 20148, for supporting this research.

Appendix A. Supplementary data

Supplementary data to this article can be found online at <https://doi.org/10.1016/j.geomorph.2026.110335>.

Data availability

Cross-section (.xlsx) and MATLAB code (.docx) to compute *BRI** are in Supplementary Material; DSMs and orthophotos are on Zenodo (10.5281/zenodo.17422937).

References

- Ashmore, P., 2013. Morphology and dynamics of braided rivers. In: *Treatise on Geomorphology*. Elsevier, pp. 289–312. <https://doi.org/10.1016/B978-0-12-374739-6.00242-6>.
- Ashmore, P., Sauks, E., 2006. Prediction of discharge from water surface width in a braided river with implications for at-a-station hydraulic geometry. *Water Resour. Res.* 42.
- Belletti, B., Dufour, S., Piégay, H., 2013. Regional variability of aquatic pattern in braided reaches (example of the French Rhône basin). *Hydrobiologia* 712, 25–41.
- Belletti, B., Dufour, S., Piégay, H., 2015. What is the relative effect of space and time to explain the braided river width and island patterns at a regional scale? *River Res. Appl.* 31, 1–15. <https://doi.org/10.1002/rra.2714>.
- Bridge, J.S., 1993. The interaction between channel geometry, water flow, sediment transport and deposition in braided rivers. *Geol. Soc. Spec. Publ.* 75, 13–71.
- Brousse, G., Liébault, F., Arnaud-Fassetta, G., Breilh, B., Tacon, S., 2021. Gravel replenishment and active-channel widening for braided-river restoration: The case of the Upper Drac River (France). *Sci. Total Environ.* 766, 142517. <https://doi.org/10.1016/j.scitotenv.2020.142517>.
- Carrivick, J.L., Heckmann, T., 2017. Short-term geomorphological evolution of proglacial systems. *Geomorphology* 287, 3–28. <https://doi.org/10.1016/j.geomorph.2017.01.037>.
- Carrivick, J.L., Rushmer, E.L., 2009. Inter- and intra-catchment variations in proglacial geomorphology: an example from Franz Josef Glacier and Fox Glacier, New Zealand. *Arct. Antarct. Alp. Res.* 41, 18–36. <https://doi.org/10.1657/1523-0430-41.1.18>.
- Carrivick, J.L., Russell, A.J., 2013. Glacial landforms, sediments | glaciofluvial landforms of deposition. In: Elias, S.A., Mock, C.J. (Eds.), *Encyclopedia of Quaternary Science* (Second Edition). Elsevier, Amsterdam, pp. 6–17. <https://doi.org/10.1016/B978-0-444-53643-3.00083-2>.
- Carrivick, J.L., Tweed, F.S., 2013. Proglacial lakes: character, behaviour and geological importance. *Quat. Sci. Rev.* 78, 34–52. <https://doi.org/10.1016/j.quascirev.2013.07.028>.
- Carrivick, J.L., Heckmann, T., Turner, A., Fischer, M., 2018. An assessment of landform composition and functioning with the first proglacial systems dataset of the central European Alps. *Geomorphology* 321, 117–128. <https://doi.org/10.1016/j.geomorph.2018.08.030>.
- Chapuis, M., Elabas, A.A., Souriguère, K., Compagnon, F., Mayen, V., Terrier, B., 2018. Quantification of the morphodynamics and ecological functionality of a Mediterranean river. In: *E3S Web of Conferences*, p. 2042.
- Corte, E., Ajmar, A., Camporeale, C., Cina, A., Coviello, V., Giulio Tonolo, F., Godio, A., Macelloni, M.M., Tamea, S., Vergnano, A., 2024. Multitemporal characterization of a proglacial system: a multidisciplinary approach. *Earth Syst. Sci. Data* 16, 3283–3306. <https://doi.org/10.5194/essd-16-3283-2024>.
- De Jong, C., 1992. Thresholds for channel change on two contrasting pro-glacial river fans, West Greenland. *Geogr. Ann. Ser. A Phys. Geogr.* 74, 1–12. <https://doi.org/10.1080/04353676.1992.11880344>.
- Delaney, I., Bauder, A., Huss, M., Weidmann, Y., 2018. Proglacial erosion rates and processes in a glacierized catchment in the Swiss Alps. *Earth Surf. Process. Landf.* 43, 765–778. <https://doi.org/10.1002/esp.4239>.
- Delaney, I., Werder, M.A., Felix, D., Albayrak, I., Boes, R.M., Farinotti, D., 2024. Controls on sediment transport from a glacierized catchment in the Swiss Alps established through inverse modeling of geomorphic processes. *Water Resour. Res.* 60, e2023WR035589. <https://doi.org/10.1029/2023WR035589>.
- Devreux, L., Chapuis, M., Belletti, B., 2022. Hydromorphological analysis on restored Alpine braided rivers. *Geomorphology* 415, 108404. <https://doi.org/10.1016/j.geomorph.2022.108404>.
- Dirszowsky, R.W., Desloges, J.R., 2004. Evolution of the Moose Lake Delta, British Columbia: implications for Holocene environmental change in the Canadian Rocky Mountains. *Geomorphology* 57, 75–93. [https://doi.org/10.1016/S0169-555X\(03\)00084-9](https://doi.org/10.1016/S0169-555X(03)00084-9).
- Egozi, R., Ashmore, P., 2008. Defining and measuring braiding intensity. *Earth Surf. Process. Landf.* 33, 2121–2138.
- Ferguson, R.I., 1993. Understanding braiding processes in gravel-bed rivers: progress and unsolved problems. *Geol. Soc. Spec. Publ.* 75, 73–87. <https://doi.org/10.1144/GSL.SP.1993.075.01.03>.
- Friend, P.F., Sinha, R., 1993. Braiding and meandering parameters. *Geol. Soc. Spec. Publ.* 75, 105–111.
- Galloway, W.E., 1991. Fan-delta, braid delta and the classification of delta systems. *Acta Geol. Sin. - Eng. Ed.* 4, 387–400. <https://doi.org/10.1111/j.1755-6724.1991.mp4004004.x>.
- Gob, F., Thommeret, N., Bilodeau, C., Tamisier, V., Rivière, R., Kreutzenberger, K., 2025. Assessing the morphological alteration of river reaches from 15 years of measurements: French hydromorphological database and indicators (Carhyce). *Geomorphology* 479, 109737. <https://doi.org/10.1016/j.geomorph.2025.109737>.
- Hoey, T.B., Sutherland, A.J., 1991. Channel morphology and bedload pulses in braided rivers: a laboratory study. *Earth Surf. Process. Landf.* 16, 447–462. <https://doi.org/10.1002/esp.3290160506>.
- Kruskal, W.H., Wallis, W.A., 1952. Use of ranks in one-criterion variance analysis. *J. Am. Stat. Assoc.* 47, 583–621. <https://doi.org/10.1080/01621459.1952.10483441>.
- Lallias-Tacon, S., Liébault, F., Piégay, H., 2017. Use of airborne LIDAR and historical aerial photos for characterising the history of braided river floodplain morphology and vegetation responses. *Catena* 149, 742–759. <https://doi.org/10.1016/j.catena.2016.07.038>.
- Le Hooke, R.B., Rohrer, W.L., 1979. Geometry of alluvial fans: effect of discharge and sediment size. *Earth Surf. Process.* 4, 147–166. <https://doi.org/10.1002/esp.3290040205>.
- Le Men, H., Trévisan, J., Boldo, D., 2002. Automatic extraction of landcover themes on digital orthophos in mountainous area for mapping at 1/25k. *Int. Arch. Photogramm. Remote. Sens. Spat. Inf. Sci.* 34, 331–338.
- Liébault, F., Lallias-Tacon, S., Cassel, M., Talaska, N., 2013. Long profile responses of alpine braided rivers in SE France. *River Res. Appl.* 29, 1253–1266. <https://doi.org/10.1002/rra.2615>.
- Macelloni, M.M., Corte, E., Ajmar, A., Cina, A., Giulio Tonolo, F., Maschio, P.F., Pisoni, I.N., 2022. Multi-platform, Multi-scale and Multi-temporal 4D Glacier Monitoring. The Rutor Glacier Case Study. Springer, Cham, pp. 392–404. https://doi.org/10.1007/978-3-031-17439-1_29.
- Maizels, J., 2002. 9 - Sediments and landforms of modern proglacial terrestrial environments. In: Menzies, J. (Ed.), *Modern and Past Glacial Environments*. Butterworth-Heinemann, Oxford, pp. 279–316. <https://doi.org/10.1016/B978-075064226-2/50012-X>.
- Mancini, D., Dietze, M., Müller, T., Jenkin, M., Miesen, F., Roncoroni, M., Nicholas, A.P., Lane, S.N., 2023. Filtering of the signal of sediment export from a glacier by its proglacial forefield. *Geophys. Res. Lett.* 50, e2023GL106082. <https://doi.org/10.1029/2023GL106082>.
- Mancini, D., Roncoroni, M., Dietze, M., Jenkin, M., Müller, T., Ouvry, B., Miesen, F., Pythoud, Q., Hofmann, M., Lardet, F., Nicholas, A.P., Lane, S.N., 2024. Rates of evacuation of bedload sediment from an Alpine glacier control proglacial stream morphodynamics. *Case Rep. Med.* 129, e2024JF007727. <https://doi.org/10.1029/2024JF007727>.
- Mancini, D., Nicholas, A.P., Roncoroni, M., Müller, T., Jenkin, M., Miesen, F., Dietze, M., Calvo, F., Lane, S.N., 2025. Simulation of proglacial forefield morphodynamics and their implications for the filtering of subglacial sediment export following glacier retreat. *Earth Surf. Process. Landf.* 50, e70143. <https://doi.org/10.1002/esp.70143>.
- Matthews, J.A., 2019. Geomorphology of proglacial systems: landform and sediment dynamics in recently deglaciated Alpine landscapes. *The Holocene*. <https://doi.org/10.1177/0959683619840576>.
- Montgomery, D.R., Buffington, J.M., 1997. Channel-reach morphology in mountain drainage basins. *GSA Bull.* 109, 596–611. [https://doi.org/10.1130/0016-7606\(1997\)109<0596:CRMIMD>2.3.CO;2](https://doi.org/10.1130/0016-7606(1997)109<0596:CRMIMD>2.3.CO;2).

- Morche, D., Schuchardt, A., Dubberke, K., Baewert, H., 2015. Channel morphodynamics on a small proglacial braid plain (Fagge River, Gepatschferner, Austria). *Proc. Int. Assoc. Hydrol. Sci.* 367, 109–116. <https://doi.org/10.5194/piahs-367-109-2015>.
- Morel, M., Tamisier, V., Pella, H., Booker, D.J., Navratil, O., Piégay, H., Gob, F., Lamouroux, N., 2019. Revisiting the drivers of at-a-station hydraulic geometry in stream reaches. *Geomorphology* 328, 44–56.
- Normandeau, A., Dietrich, P., Hughes Clarke, J., Van Wychen, W., Lajeunesse, P., Burgess, D., Ghienne, J.-F., 2019. Retreat pattern of glaciers controls the occurrence of turbidity currents on high-latitude Fjord Deltas (Eastern Baffin Island). *Case Rep. Med.* 124, 1559–1571. <https://doi.org/10.1029/2018JF004970>.
- Patranabis-Deb, S., Chaudhuri, A.K., 2007. A retreating fan-delta system in the Neoproterozoic Chattisgarh rift basin, central India: Major controls on its evolution. *Am. Assoc. Pet. Geol. Bull.* 91, 785–808. <https://doi.org/10.1306/11270605182>.
- Piermattei, L., Heckmann, T., Betz-Nutz, S., Altmann, M., Rom, J., Fleischer, F., Stark, M., Haas, F., Ressler, C., Wimmer, M.H., Pfeifer, N., Becht, M., 2023. Evolution of an Alpine proglacial river during 7 decades of deglaciation. *Earth Surf. Dyn.* 11, 383–403. <https://doi.org/10.5194/esurf-11-383-2023>.
- Pitlick, J., Mueller, E.R., Segura, C., Cress, R., Torizzo, M., 2008. Relation between flow, surface-layer armoring and sediment transport in gravel-bed rivers. *Earth Surf. Process. Landforms* 33, 1192–1209.
- Sanders, J.W., Cuffey, K.M., MacGregor, K.R., Collins, B.D., 2013. The sediment budget of an Alpine cirque. *Bull. Geol. Soc. Am.* 125, 229–248. <https://doi.org/10.1130/B30688.1>.
- Savi, S., Pitscheider, F., Engel, M., Coviello, V., Strecker, M.R., Comiti, F., 2024. Sediment export from an Alpine proglacial area under a changing climate: budgets, rates, and geomorphological processes. *Geomorphology* 462, 109343. <https://doi.org/10.1016/j.geomorph.2024.109343>.
- Šidák, Z., 1967. Rectangular confidence regions for the means of multivariate normal distributions. *J. Am. Stat. Assoc.* 62, 626–633. <https://doi.org/10.1080/01621459.1967.10482935>.
- Terrier, B., Piégay, H., Lébault, F., Dufour, S., Belletti, B., Le Lay, Y.F., Marmonier, P., Comby, E., Tacon, S., Faton, J.M., et al., 2019. Les rivières en tresses: Éléments de connaissances. Eau & Connaissance, Agence l'Eau Rhône-Méditerranée-Corse, Lyon (118p).
- Tetteh, G.O., Schönert, M., 2015. Automatic generation of water masks from rapideye images. *J. Geosci. Environ. Prot.* 3, 17–23.
- Toone, J., Rice, S.P., Piégay, H., 2014. Spatial discontinuity and temporal evolution of channel morphology along a mixed bedrock-alluvial river, upper Drôme River, southeast France: Contingent responses to external and internal controls. *Geomorphology* 205, 5–16. <https://doi.org/10.1016/j.geomorph.2012.05.033>.
- Villa, F., De Amicis, M., Maggi, V., 2007. GIS analysis of Rutor Glacier (Aosta Valley, Italy) volume and terminus variations. *Geogr. Fis. Din. Quat.* 30, 87–95.
- Winsemann, J., Lang, J., Polom, U., Loewer, M., Igel, J., Pollak, L., Brandes, C., 2018. Ice-marginal forced regressive deltas in glacial lake basins: geomorphology, facies variability and large-scale depositional architecture. *Boreas* 47, 973–1002. <https://doi.org/10.1111/bor.12317>.